Full length article

Non-conservative dynamics of lattice sites near a migrating interface in a diffusional phase transformation

T. Yang [a, b, 1], Y. Gao [c, 1], D. Wang [a], R.P. Shi [c], Z. Chen [b], J.F. Nie [d], J. Li [a, e, f], Y. Wang [a, c, *]

[a] Center of Microstructure Science, Frontier Institute of Science and Technology, State Key Laboratory for Mechanical Behavior of Materials, Xi'an Jiaotong University, Xi'an, 710049, China
[b] State Key Laboratory of Solidification Processing, Northwestern Polytechnical University, Xi'an, 710049, China
[c] Department of Materials Science and Engineering, The Ohio State University, Columbus, OH, 43210, USA
[d] Department of Materials Science and Engineering, Monash University, Clayton, Victoria, 3800, Australia
[e] Department of Nuclear Science and Engineering, Massachusetts Institute of Technology, Cambridge, MA, 02139, USA
[f] Department of Materials Science and Engineering, Massachusetts Institute of Technology, Cambridge, MA 02139, USA

ARTICLE INFO

ABSTRACT

Migration of phase boundaries in crystalline solids eliminates one set of lattice sites and establishes another. Using a combination of phase field crystal modeling and crystallographic analysis, we present here a complete atomistic description of the migration mechanism of a high-index planar interface during a diffusional hexagon to square phase transformation. In particular we show that a terrace-step interface advances macroscopically in the form of growth ledges, while microscopically its migration occurs by opposite shearing on the terraces and a *one-to-two splitting* of lattice sites, giving a new class of lattice site correspondence and superabundant vacancies. In addition, a new approach capable of finding a critical nucleus with atomic resolution is developed by combining the phase field crystal energetics with the free-end nudged elastic band algorithm.

© 2017 Acta Materialia Inc. Published by Elsevier Ltd. All rights reserved.

1. Introduction

When people invoke "atoms" to describe plasticity or phase transformation of crystalline materials, they very often really mean "atomic sites" (lattice site or site in this paper). The distinction between "site" and "atom" is parallel to the distinction between the governmental structure of a country and who is occupying which office at the moment. "Site" can be enduring, for instance a particular lattice site in bronze may be occupied by Cu atom, Sn atom or vacancy at different times. However, in plasticity and in phase transformations, the site lattice may necessarily change. Unlike atoms which cannot be created/annihilated and therefore must satisfy local conservation, there is no conservation rule of lattice sites, so concepts like "lattice correspondence", "ledge motion" and "transformation strain" need to be carefully considered in light of this [1]. Here we examine the creation/annihilation/motion dynamics of lattice sites in a model hexagon-to-square lattice phase

transformation, and try to address the fundamental question of "where, when and how does lattice site arise?"

Interfaces play essential roles in microstructural evolution [2,3]. Compared to crystallographic theories of interface structures [4–13], how these interfaces migrate in plasticity and phase transformation is less clear. The structure of a phase boundary dictated by the invariant plane strain (IPS) condition consists of terraces and steps, referred to as structural ledges (SLs) or disconnections. It is often assumed that a *collective* motion of SLs within the terrace plane accounts for the advance of the macroscopic interface [3,10,13]. Chiao and Chen [10] reported that the steps/ledges of the orthorhombic/monoclinic interface move synchronously as an entity. This view has been followed by Pond and Hirth [13] and is also accepted in the Book by Sutton and Balluffi [3]. But the Moiré ledge (ML) approach suggests that, an extrinsic ledge, defined as the ML between two adjacent Moiré planes, could be responsible for the migration of a terrace-step interface [14–16].

Moreover, the practice of one-to-one lattice site correspondence, which is implicitly assumed in all ledge-wise migration mechanisms [17,18], may not be satisfied. This is where the confusion between "site" and "atom" tends to cause trouble. While an atom can only be at one place at a time, a "site" can move, split

---

into two, or be eliminated when a phase boundary sweeps across. This is because a site is just the location where there is significant probability of finding an atom, so an atom occupying an old site, when that old site is eliminated, can find itself presented with two new sites nearby (in the one-to-two splitting case) with certain probability to migrate to, like in quantum mechanics. For example, if there is a significant molar volume difference between the product and matrix phases, the number of lattice sites before and after the transformation might be different. In order to accommodate the molar volume change, creation or annihilation of lattice sites becomes necessary, such as the formation of a large amount of excess vacancies observed in the ordering processes of Ni$_3$Fe and Cu$_3$Au [19]. "Superabundant vacancies" is therefore one way to reconcile the conservation of mass with the non-conservation of sites when the phase boundary sweeps across. Crystal displacements $\mathbf{u}(\mathbf{r})$ like in the Kirkendall effect [20] or elastic strain $\varepsilon(\mathbf{r})$ (and stress $\sigma(\mathbf{r})$) are other ways of accommodating the large molar volume change.

In this paper, combining the phase field crystal (PFC) method [21–24], theory of crystallography [6,8,11,14] and nudged elastic band method (NEB) [25,26], we investigate the atomistic mechanisms of interface migration during a model diffusional phase transformation from hexagon lattice to square lattice with large molar volume differences. Relying on a properly time-averaged atomic density field [27], PFC can capture lattice site movements at diffusional time scale [28–30]. Theories of O-line, SL and coincidence site lattice (CSL) are used to analyze the structure of interfaces. In order to obtain a complete picture of the phase transformation including nucleation and growth, a new approach capable of capturing the critical nucleus configuration with atomic resolution is developed by combining the free-end NEB algorithm [25,26] with PFC energetics.

Note that as a general phenomenon of pattern formation and evolution, the square to hexagon transformation has been studied extensively in the literature [31–37], but the focus of the current study is completely different, with particular emphases on (i) when the orientation relationship between the parent and product phases is formed (e.g., during nucleation or growth), (ii) detailed atomic arrangement at the interface including steps, terraces and dislocation structures, (iii) how a high-index terrace-step interface moves (e.g., via structural ledge or ML), (iv) whether the commonly assumed one-to-one lattice site correspondence holds, and (v) how the large volume change is accommodated.

2. Methods

2.1. Phase field crystal model

The PFC model uses the Helmholtz free energy to describe an inhomogeneous system in reference to a homogenous liquid state of density ρ_L and the dimensionless form of the Helmholtz free energy is given as [23],

$$F_{PFC} = \int \left\{ \left[\frac{n(\mathbf{r})^2}{2} - \eta \frac{n(\mathbf{r})^3}{6} + \nu \frac{n(\mathbf{r})^4}{12} \right] - \left[\frac{1}{2} n(\mathbf{r}) \int C_2(|\mathbf{r} - \mathbf{r}'|) n(\mathbf{r}') d\mathbf{r}' \right] \right\} d\mathbf{r} \tag{1}$$

where $n(\mathbf{r}) \equiv \rho(\mathbf{r})/\rho_L - 1$ is the dimensionless number density field. Parameters η and ν are the expansion coefficients and they are assumed unity (i.e., $\eta = \nu = 1$) in the current study. The direct pair correlation function $C_2(|\mathbf{r} - \mathbf{r}'|)$ is constructed by the envelope of two Gaussian peaks in the reciprocal space as [23],

$$\widehat{C}_2(|\mathbf{k}|) = \begin{cases} e^{-\frac{T^2 k_1^2}{2\rho_1 \beta_1}} e^{-\frac{(|\mathbf{k}| - k_1)^2}{2a_1^2}}, & |\mathbf{k}| \leq k_c \\ e^{-\frac{T^2 k_2^2}{2\rho_2 \beta_2}} e^{-\frac{(|\mathbf{k}| - k_2)^2}{2a_2^2}}, & |\mathbf{k}| > k_c \end{cases} \tag{2}$$

where k_c is the intersection point of the two peaks. The wave vector $k_1 = 2\pi$, $k_2 = \sqrt{2}k_1$, and other symmetry-related parameters ρ_i and β_i ($i = 1, 2$) are determined in accordance with a square lattice [23]. Depending on temperature T, the contribution from different peaks varies, thus leading to the formation of a hexagon phase at high temperature where the first peak dominates and a square phase at low temperature where both peaks play a role.

The phase diagram is determined by common tangent construction on the free energy curves of different phases at each temperature. In particular, the free energy of the liquid phase is calculated by imposing a constant density field with $n_{liq} = \overline{n}$. For the solid phases, the density field for the square lattice is represented using a two-mode approximation,

$$n_{sq} = \overline{n} + 2A_{sq}^1 \left[\cos(k_{sq}x) + \cos(k_{sq}y) \right] + 4A_{sq}^2 \cos(k_{sq}x)\cos(k_{sq}y) \tag{3}$$

and the density field for the hexagon lattice is represented by a one-mode approximation,

$$n_{hex} = \overline{n} + 4A_{hex} \cos(k_{hex}x)\cos\left(k_{hex}y / \sqrt{3}\right) - 2A_{hex} \cos\left(2k_{hex}y / \sqrt{3}\right) \tag{4}$$

where the wave vectors $k_{sq} = k_1$ and $k_{hex} = 2/\sqrt{3}k_1$. The amplitudes A_{sq}^1, A_{sq}^2 and A_{hex} can be obtained by free energy minimization. Analytic expressions of the free energy densities for all the phases are presented in Appendix A, and the resultant phase diagram is shown in Fig. 1.

The transformation and interface migration are characterized by the time-evolution of the atomic number density field $n(\mathbf{r})$ that is governed by the conserved equation of motion,

$$\frac{\partial n}{\partial t} = \nabla^2 \frac{\delta F_{PFC}}{\delta n} + \xi \tag{5}$$

where ξ represents a colored Gaussian noise described by
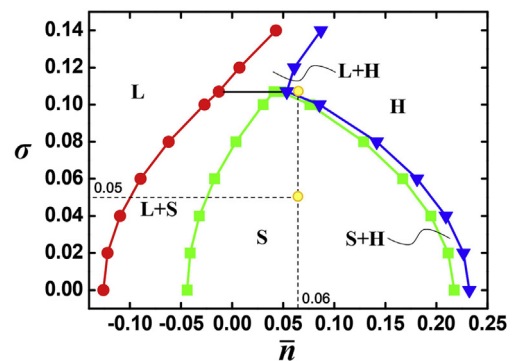
Fig. 1. Phase diagram constructed by using the free energy model presented in the text, showing phase equilibria among the liquid (L), square (S), and hexagon (H) phases. The yellow circles denote the system and temperatures considered in the simulations. (For interpretation of the references to colour in this figure legend, the reader is referred to the web version of this article.)

$$\langle \xi(\boldsymbol{r},t)\xi(\boldsymbol{r}',t') \rangle = -\alpha \nabla^2 g(|\boldsymbol{r} - \boldsymbol{r}'|, \lambda)\delta(t - t') \tag{6}$$

where α is the noise strength and $g(|\boldsymbol{r} - \boldsymbol{r}'|, \lambda)$ is a high frequency cutoff function for wavelengths shorter than the atomic spacing λ [24]. This equation is solved numerically using a semi-implicit technique in the reciprocal space, assuming a periodic boundary condition in 2D. Miller-Bravais index notation is used for the hexagon crystal to preserve the permutation symmetry.

2.2. Free-end nudged elastic band method

As compared with the conventional nudged elastic band (NEB) algorithm [38], the free-end NEB (FE-NEB) method chooses a partially transformed state (instead of a fully transformed one) as the end node, by which the efficiency and accuracy can be improved significantly [25,26]. In the implementation of FE-NEB, an elastic band consisting of K nodes, denoted as $[\boldsymbol{R}_1, \boldsymbol{R}_2, \ldots, \boldsymbol{R}_K]$, is firstly constructed by linear interpolation between $\boldsymbol{R}_1$ and $\boldsymbol{R}_K$ states, where the microstructural configurations of the first node and the end node are provided by PFC simulations. Then each node is relaxed subject to a total force consisting of a spring-type force and a potential force [25,26],

$$\boldsymbol{F}_i = \boldsymbol{F}_i^S\big|_{\parallel} + \boldsymbol{F}_i^P\big|_{\perp}, \ i = 1, \ldots, K, \tag{7}$$

where the subscripts $\parallel$ and $\perp$ represent the parallel and perpendicular components of forces resolved on the local tangent of each node, which is evaluated from the energy of the node and its immediate neighbors along the chain [39]. The potential force, $\boldsymbol{F}_i^P$, in the context of PFC is given by the first variation of the grand potential, $-\delta \Phi_{PFC}/\delta n$, where Φ_{PFC} is constructed through a Legendre transformation of the PFC free energy,

$$\Phi_{PFC}(\mu, V, T) = F_{PFC}(N, V, T) - \mu_0 C, \tag{8}$$

where μ_0 is the chemical potential of the reservoir and $C = \int n(r)dr$ represents the constraint of mass conservation. The spring force is defined as,

$$\boldsymbol{F}_i^S\big|_{\parallel} = k_{sp}(|\boldsymbol{R}_{i+1} - \boldsymbol{R}_i| - |\boldsymbol{R}_i - \boldsymbol{R}_{i-1}|)\boldsymbol{\tau}_i, \tag{9}$$

where k_{sp} is the spring constant and $\boldsymbol{\tau}_i$ defines the normalized local tangent on node i. In FE-NEB, the end node is allowed to move under the spring force projected on the potential energy isosurface,

$$\boldsymbol{F}_K = \boldsymbol{F}_{K,K-1}^S - \frac{\boldsymbol{F}_{K,K-1}^S \cdot \boldsymbol{F}_K^P}{\boldsymbol{F}_K^P \cdot \boldsymbol{F}_K^P}\boldsymbol{F}_K^P, \tag{10}$$

where $\boldsymbol{F}_{K,K-1}^S$ is the spring force that node $\boldsymbol{R}_{K-1}$ exerts on node $\boldsymbol{R}_K$. Thus the last node is able to swing on an energy contour until it rests on the minimum energy path (MEP). Subject to the force field $\boldsymbol{F}_i$, each node on the elastic band is relaxed iteratively until convergence is reached. During every relaxation step, elastic constant of the band and the force field are simultaneously updated as well.

3. Results

In the simulations, a single hexagon crystal is prepared first at high temperature ($T = 0.107$) using the one-mode approximation, and then quenched into the square phase field of the phase diagram ($T = 0.05$) as shown in Fig. 1. Relaxation using PFC dynamics

is performed at each stage. Colored noise term [24] is used to initiate the transformation. For a better visualization, data generated from the PFC simulation are converted into discrete lattice sites by extracting the peak positions in the density field $n(\boldsymbol{r})$ (Fig. 2). Sites at the interface in Fig. 2 are colored red, and three variants of the square phase with misorientation $\theta = 0°$ (a), $-30°$ (b) and $-60°$ (c) with respect to the matrix hexagon phase are observed, leading to an orientation relationship of $<2\overline{1}\overline{1}>_{hex}//<10>_{sq}$ established between the hexagon and square phases. For convenience, only the results associated with the first variant shown in Fig. 2(a) will be discussed hereafter because results from the other two variants are completely equivalent.

Another interesting observation is the well-faceted morphology developed at later stages as shown in Fig. 3. As will be shown later, this is closely related to the fact that the interfacial energy is reduced significantly by forming the facets. For the sake of easy analysis, the precipitate shape is displayed by using an average density profile [40], where the inclinations of the habit plane with respect to the x-axis are determined to be $\varphi_i = \pm 15°$ ($i = 1, 2$). In addition, it is also revealed that the atomic structure of the interface between the hexagon and square phases consists of terraces and steps, as shown by the inset of Fig. 3(a). The details of the crystallography analysis, including the orientation relationship, habit plane inclination and interface structure will be presented in Section 4.

In order to determine exactly when such an orientation relationship is formed, we use the free-end NEB method to search for the atomic configuration of the critical nucleus, where a supercritical nucleus obtained from the PFC simulation is used as the input of the end image. As revealed by the atomic configurations along the minimum energy path (MEP) shown in Fig. 3(b), the orientation relationship is exactly $<2\overline{1}\overline{1}>_{hex}//<10>_{sq}$. Thus, during the structural transformation the orientation relationship between the parent and product phases is formed "by birth" during nucleation and remains unchanged thereafter during growth.

To further examine how the interphase boundary plane migrates during the phase transformation, a planar interface with the habit plane orientation and structure found in the simulation (e.g., the inset in Fig. 3(a)) is created as the initial configuration (Fig. 4(a)). In order to obtain a fully relaxed interface, a small slab of supercooled liquid is placed in between the hexagon and square crystals at temperature $T = 0.05$. The interface forms when the two crystals grow and impinge upon each other, which is then evolved for a while before examination. To initiate the migration of the interface, a colored noise is used. See Supplemental Movie for the interface migration displayed using the continuous atomic density field $n(\boldsymbol{r})$.

Supplementary video related to this article can be found at http://dx.doi.org/10.1016/j.actamat.2017.01.036.

As shown in Fig. 4(b), in addition to the SLs on the interface, a growth ledge (GL) is formed in a manner similar to the double-kink nucleation mechanism seen in dislocation glide. The characteristics of both the SL and GL will be analyzed in the next section. As shown in Fig. 4 (b)-(d), through the lateral movement of the GL, the interface migrates in the normal direction from right to left. As an extrinsic part of the interface, the GL can move independently without any structural restrictions and thus fewer sites are involved during the interface migration, making it more energetically favorable as compared to the synchronized motion of all SLs. It is noticed that although structurally the GL is similar to the ML, the atomic mechanism during migration of these ledges are of fundamental difference, as explained below.
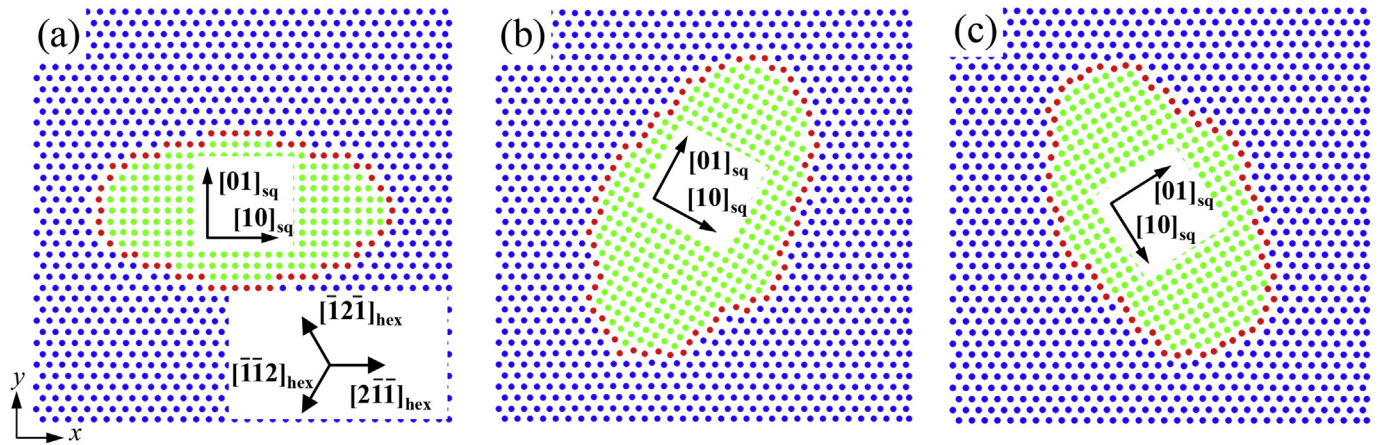
Fig. 2. Atomic configurations obtained from PFC simulations, with the square phase having misorientation $\theta = 0°$ (a), $-30°$ (b) and $-60°$ (c) with respect to the parent hexagon phase. The misorientation θ is defined by the intersection angle between the $[10]_{sq}$ direction and x-axis.
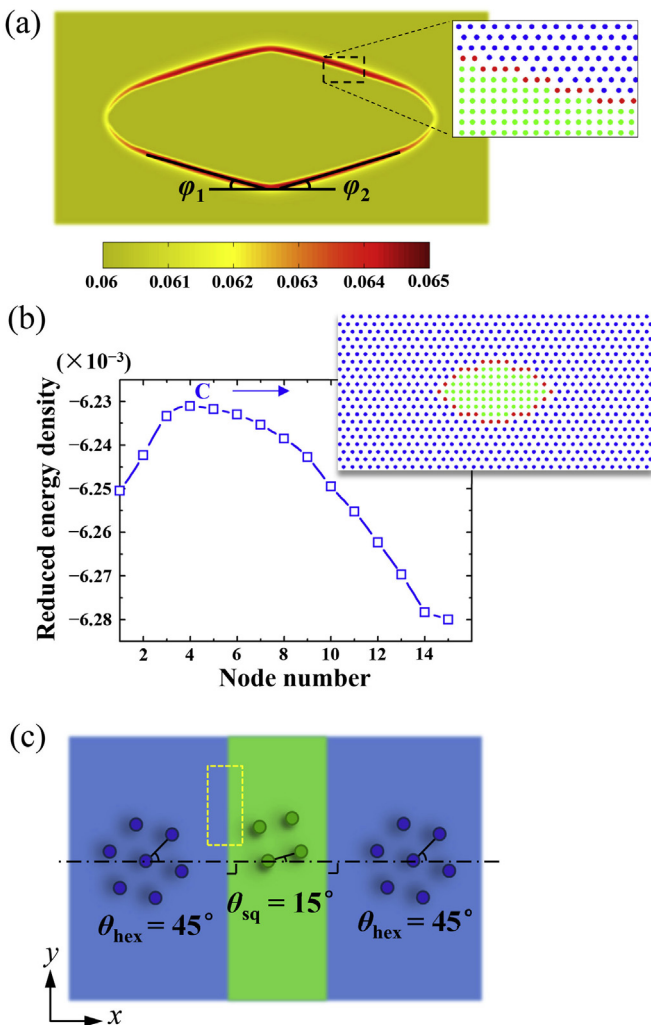
Fig. 3. (a) Shape of a square-phase precipitate embedded in a hexagon matrix obtained from the PFC simulation. (b) The minimum energy path (MEP) and critical nucleus configuration (inset) obtained from the FE-NEB calculation. (c) Schematic drawing showing the simulation setup of a macroscopic planar interface with the same orientation relationship and atomic structure as those shown in (a). The inclination angle φ_i (i = 1, 2) between the habit plane and the x-axis equals to $-15°$ and $15°$, respectively. The area enclosed by the yellow dashed box in (c) corresponds to what is shown in Fig. 4. (For interpretation of the references to colour in this figure legend, the reader is referred to the web version of this article.)

4. Discussion

4.1. Crystallographic analysis

In this section, crystallographic features exhibited during the hexagon to square transformation, including orientation relationship, habit plane inclination and interface structure, are analyzed by means of the O-line, SL and coincidence site lattice (CSL) theories [6,8,14–16,41–44]. In the formulation proposed by Zhang and Purdy [11,41], the O-line condition can be identified using a more general criterion, i.e., the Δg parallelism rule, deduced from the condition that misfit dislocations at the interface are completely eliminated in one direction. According to group theory, the number of transformation variants or deformation variants (DVs) is determined by the order of the symmetry group of the parent phase divided by the order of the so-called stabilizer group (i.e., the group includes all the unbroken symmetry operations during the transformation) for a given lattice correspondence (LC) [45]. Since the point groups of the hexagon and square phases are 6 mm and 4 mm with the order of 12 and 8 and the stabilizer group (i.e., intersection group) between them is 2 mm with the order 4, three DVs are expected. Required by the O-line condition, each DV will be transformed into two new variants with different orientations, referred to as orientation variants (OVs), generated by two appropriate rotations. Details of the crystallographic calculations are presented in Appendix B. The calculation results in reciprocal space are shown in Fig. 5, where the diffraction patterns of the hexagon phase are superimposed onto those of the final OVs of the square phase produced by the corresponding transformation matrix $\mathbf{A}_{i,j}^*$. As shown in Fig. 5, the normal $\boldsymbol{n}$ of the habit plane is parallel to the displacement vector Δg in reciprocal space, which is defined as the difference between the normal vectors of the two correlated planes, i.e., $\Delta g = g^{hex} - g^{OV}$. Two sets of correlated planes, designated as $g_1^{hex}|g_1^{OV_i}$ and $g_2^{hex}|g_2^{OV_i}$ (i = 1–6), are indicated by the ellipses in Fig. 5. For a better visualization, the geometric relations between the hexagon matrix, the DVs and the OVs during the O-line calculation are presented in real space as shown in Fig. 6.

From Fig. 6 it can be seen that the misorientation angle θ associated with the six OVs of the square phase can be summarized as: $\theta = 0°$ for OV_1 and OV_2, $\theta = -30°$ for OV_3 and OV_4, and $\theta = -60°$ for OV_5 and OV_6, yielding the orientation relationship of $<2\overline{1}\overline{1}>_{hex}//<10>_{sq}$. In addition, the associated inclination angles φ between the habit plane and x-axis are determined to be $15°$ and $-15°$ for $\theta = 0°$, $75°$ and $45°$ for $\theta = -30°$, and $-75°$ and $-45°$
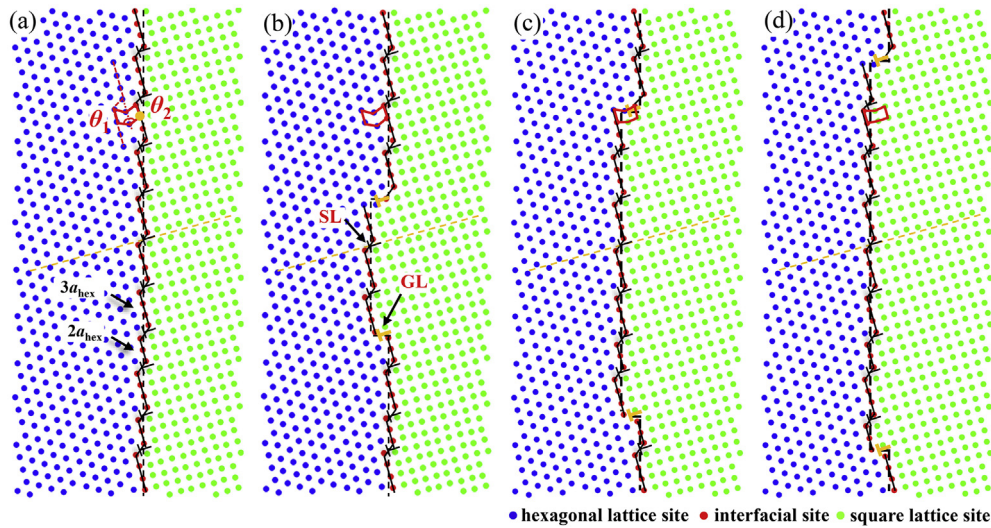
Fig. 4. Atomic configurations of a hexagon-square phase interface at different time moments during the transformation process: (a) dimensionless time $t = 10900$, (b) $t = 11650$, (c) $t = 12050$, (d) $t = 12200$. The solid and dashed black lines indicate the microscopic stepped interface and the macroscopic planar interface, respectively. The red dashed line in (a) mark the unit height of the growth ledge. The climb trajectory of the interface dislocations is represented by the gold dashed line. See Supplemental Movie M1 for the interface migration process. (For interpretation of the references to colour in this figure legend, the reader is referred to the web version of this article.)

for $\theta = -60°$, respectively. Note that OV$_1$ and OV$_2$ are non-distinguishable in terms of the misorientation between the two phases, without knowing the transformation path (i.e., lattice correspondence). However, the habit planes they form are different. It is the same for OV$_3$/OV$_4$, OV$_5$/OV$_6$. Therefore, both the orientation relationship and the habit plane inclination established during the hexagon to square transformation are well captured by our simulation and are in a good accordance with the crystallographic analysis.

For the atomic configurations of the interface, since the boundary plane inclination $\varphi = \pm 15°$ is irrational with respect to both phases, a stepped interface consisting of terraces and steps (as indicated by the black lines in Fig. 7(a)) develops in order to guarantee the optimal atomic site matching along the interface, which is indicated by the appearance of periodical good-matching (relatively) patches of atomic sites (gold-colored) in Fig. 7(a). For convenience, a criterion is set for "good-matching", i.e., pairs of sites are regarded as good-matching if their separation is below 15% of the spacing between adjacent [01]$_{sq}$ rows, similar to that used in the literature [41,42]. Based on the crystallographic relationship shown in Fig. 7(b), the (average) terrace length l_{SL} defined in the hexagon lattice equals to $l_{SL} = h_{SL}\cot\varphi - h_{SL}\cot 60°$, where h_{SL} represents the step height. With $h_{SL} = 1$ and $\varphi = 15°$, the length of the terraces l_{SL} is determined to be 3.155. Because the terrace length l_{SL} is not an integer number of the atomic spacing along $[2\overline{1}\overline{1}]_{hex}$, the combination of two sets of terraces with length $3a_{hex}$ and $2a_{hex}$ is expected, as indicated in Fig. 4(a), where $a_{hex} = 2/\sqrt{3}$ is the lattice constant of the hexagon lattice. As will be shown later in Fig. 10, these two terrace sizes correspond to two different types of shear zones. On the other hand, in order to compensate the misfit within the terraces arising from the difference in inter-atomic distance along the $[2\overline{1}\overline{1}]_{hex}$ and $[10]_{sq}$ directions, interfacial dislocations or disconnections appear on the steps as indicated by the dislocation sign in Fig. 7(a). Based on the CSL model [43,44], the Burgers vector of the interfacial dislocations should be a displacement shift complete lattice (DSCL) vector to preserve the interface structure with the least displacement. By applying the Burgers circuit abcda' (Fig. 7(a)), the Burgers vector is determined to be $1/6[2\overline{1}\overline{1}]_{hex}|1/2[10]_{sq}$, where the DSCL is indicated by the dashed red lines in Fig. 7(a) [41].

Fig. 8 shows the atomic structure of the GL appeared during the interface migration process simulated by the PFC (Fig. 4). The unit height of the GL, h_{GL}, which is defined as the spacing between two neighboring habit planes, is equivalent to $2h_{SL}$ based on the calculation in Appendix B, as shown in Fig. 8. Two sets of planes, $(10)_{OV_2}|(\overline{1}10)_{hex}$ planes and $(01)_{OV_2}|(01\overline{1})_{hex}$ planes, intersect at the same interface, indicating an energy minimum associated with the habit plane [11]. Here the GL can be regarded as a ML since the habit planes containing the invariant lines are equivalent to the Moiré planes and the unit height of the GL can also be obtained from the ML analysis [14–16].

4.2. Critical nucleus configuration by FE-NEB method

Because of the statistical nature of Langevin dynamics (Eq. (5)), it is difficult to use it in the PFC model to search for the exact saddle configuration. In addition, an artificially large amplitude of the noise term has usually to be adapted in order to capture the nucleation events within a computationally affordable time interval. By combing the ability of the FE-NEB technique [25,26] to search for saddle point configurations along the MEP and the Langevin dynamics in PFC to generate an over critical configuration as the free-end image, we show that the critical nucleus configuration with atomistic resolution and the associated activation energy can be easily obtained. For the hexagon-to-square transformation considered in the current study, the critical nucleus configuration obtained using this approach is shown in the inset of Fig. 3(b). As has been mentioned earlier, the orientation relationship between the parent and product phases for this transformation has already been formed at the birth of the square phase, $<2\overline{1}\overline{1}>_{hex}//<10>_{sq}$, where the $[10]_{sq}$ direction in the square phase is aligned with the $[2\overline{1}\overline{1}]_{hex}$ direction in the hexagon phase, offering the minimum lattice mismatch and interfacial energy between the two phases. Following the same line of arguments, critical nucleus has adopted an elliptical morphology instead of the circular ones as assumed in the classic nucleation theory.

In addition, since only the total free energy and the first-order derivatives of the PFC functional are required in the implementation of the NEB calculation, this approach can also be extended to other thermally activated processes that can be modeled by the PFC
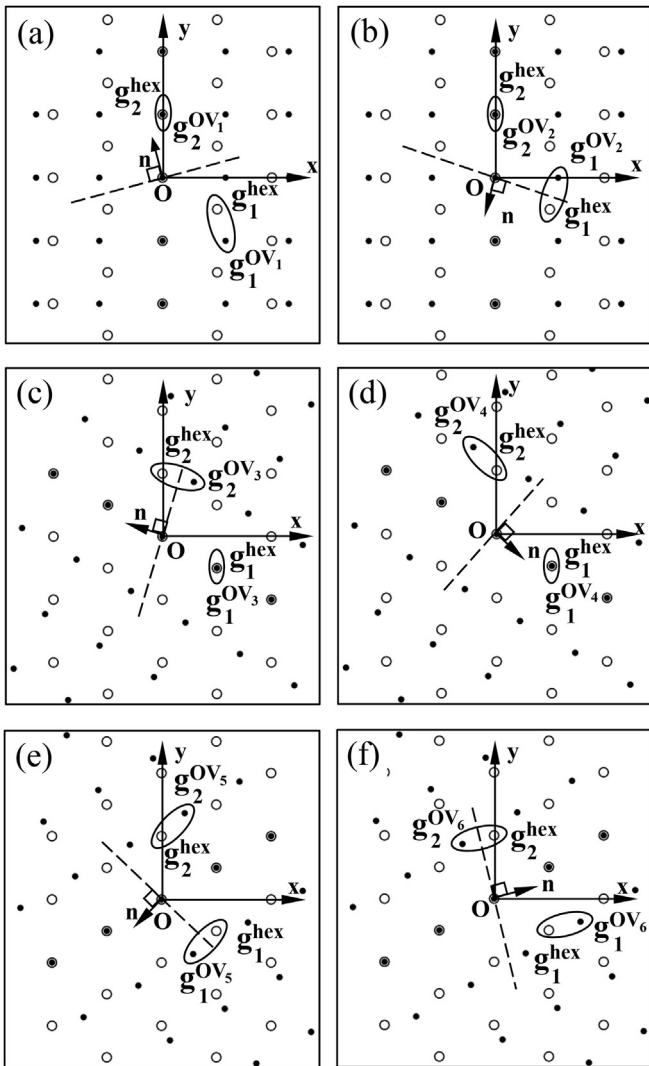
Fig. 5. Superimposed diffraction patterns of the hexagon (open circles) and square (filled circles) phases. The square phases in (a–f) correspond to the six orientation variants described in Fig. 6. Dashed lines represent the habit plane trace. Ellipses indicate the two sets of correlated principal planes, namely $\mathbf{g}_1^{hex}|\mathbf{g}_1^{OV_i}$ and $\mathbf{g}_2^{hex}|\mathbf{g}_2^{OV_i}$ ($i = 1$–6).

Fig. 6. Crystallographic relationships between the hexagon and square phases in real space. The matrix phase and the deformation variants (DVs) and orientation variants (OVs) of the square phase are colored in white, light blue and light green, respectively. Blue and green arrows indicate the corresponding lattice vector pairs in the hexagon phase and different variants of the square phase. The dashed lines denote the habit plane trace. (For interpretation of the references to colour in this figure legend, the reader is referred to the web version of this article.)

method, including nucleation of other extended defects such as dislocation loops, stacking faults, voids, et al., nucleated either homogeneously or heterogeneously.

4.3. Growth mechanism

A peculiar self-accommodation mechanism is found to operate within the unit height of the GL. Two rhombuses of mirror symmetry are outlined (in red) within a unit height of the GL in Fig. 4(a). By examining the variation of angles θ_1 and θ_2, which characterizes the shape change of these two rhombuses, the structural transformation occurring at atomistic scale is revealed. As shown in Fig. 9(a), the angles of both θ_1 and θ_2 increase gradually from $60°$ to $90°$, demonstrating the occurrence of two opposite shears during the migration process. The deviation of angles from exact values of $60°$ and $90°$ in Fig. 9(a) is caused by the spatial discretization [46] and the local lattice distortion in the close proximity to the interface. As an indicator of boundary migration, Fig. 9(b) shows the transformation of the number of nearest neighbors (NN) of the

gold-colored atomic sites in Fig. 4(a) from 6 to 5 and then to 4, indicating the completion of the hexagon to square phase transformation in the region. Accompanying the shearing process, dislocations located at the edges of the terraces are found to climb, following the trajectory depicted by the dashed gold lines in Fig. 4.

By analyzing the site movements revealed in Fig. 4, a periodic arrangement of two opposite shear modes (represented by two different colors) is shown graphically in Fig. 10. On the boundary of the shearing zones, intersection sites are identified, marked by the open-circles. Unlike the one-to-one LC in each shearing zone, a one-to-two splitting of lattice sites emerges locally among these intersection sites. Non-conservation of lattice sites has been observed in various structural transformations in experiments, for example, in the ordering processes of Ni_3Fe and Cu_3Au [19] where large lattice contractions are involved. Also, from Fig. 10, it is shown that the mode of site movement and creation (mixed-type LC) differs from the one-to-one LC that is usually assumed in the ledge-wise motion of both ML and SL mechanisms [3,10,13–15], even though the fundamental structural features (e.g., orientation relationship, habit plane inclination) of the GL predicted by PFC in this study agree well with those predicted by the existing crystallographic theories. In general, the operation of an interface migration mechanism depends not only on the structure of an interface, i.e., stepped or flat, coherent or semi-coherent or incoherent, etc., but also on many other factors such as the transformation driving force and boundary conditions, thus, leading to diverse modes of migration even for the same interface.

The particular migration mode presented above, for which site displacements $\mathbf{u}(\mathbf{r})$ away from the moving phase boundary is nearly zero (see Supplementary Movie), should be a mode observable at higher temperatures when diffusion is rampant and residual stress $\sigma(\mathbf{r})$ is small. It is in principle also possible for the vacancies to annihilate at phase boundaries to create lab-frame crystal displacements, like in the Kirkendall experiments, but this may necessitate the generation of strain and stress depending on the far-field mechanical boundary condition, and is anyhow not the main accommodation mechanism seen in the present simulations. Both modes of accommodating the lattice site density change (by superabundant vacancies or by displacement) can be considered high-temperature, low-stress, diffusion-dominant processes. As the transformation temperature lowers, at certain point the displacive character could dominate, which necessitates significant
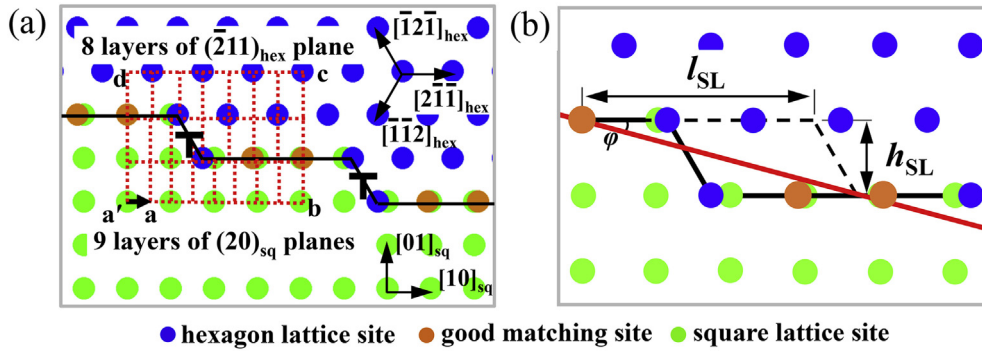
Fig. 7. Interfacial structure between the hexagon and square phases in a non-relaxed state: (a) Atom matching along the interface and dislocation arrangement, (b) the (average) terrace length l_{SL} and step height h_{SL}. Symbol 'T' denotes the misfit dislocation core at the step riser. The red line in (b) marks the inclination of the macroscopic habit plane. (For interpretation of the references to colour in this figure legend, the reader is referred to the web version of this article.)
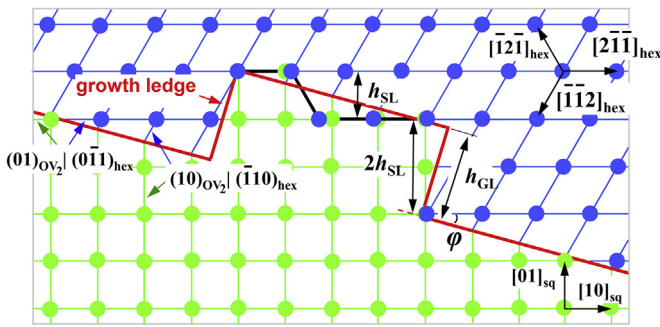
Fig. 8. Schematic drawing illustrating the atomic structure of SL and GL at the interface. The red lines represent the macroscopic habit planes and the GL, while the black lines represent the microscopic terraces and steps. The heights of both GL and SL are marked. Two sets of planes, $(01)_{OV_2} \| (01\bar{1})_{hex}$ and $(10)_{OV_2} \| (\bar{1}10)_{hex}$, intersected at the same interface, indicating an energy minimum associated with the habit plane. (For interpretation of the references to colour in this figure legend, the reader is referred to the web version of this article.)

displacement $\mathbf{u}(\mathbf{r})$ and stress $\boldsymbol{\sigma}(\mathbf{r})$ away from the migrating interface. At such low temperatures, due to the difficulty of diffusion and the increasing deterministic nature of military-style transformations, the non-conservative nature of lattice site correspondences is expected to decrease, where the lattice sites move as atoms, and do not split from one to two, or vanish, as the phase boundary sweeps across.

The mixed-type LC found in the current study emerges in two forms, named Type I in Fig. 10(a) and (b) and Type II in Fig. 10(c) and (d), which are directly related to the terrace-step interphase boundary structure. Type I is associated with the terrace length of $3a_{hex}$ while Type II is associated with the terrace length of $2a_{hex}$, and their respective volume changes are calculated to be -1.03% and 3.92%, considering the identical inter-planar spacing of the $(01\bar{1})_{hex}$ and $(01)_{sq}$ planes. Therefore, by a right mixture of these two types, e.g., 79.3% of the system undergoes the correspondence through Type I and 20.7% undergoes the correspondence through Type II, the volume change, which would otherwise reaches to 13.4% in any conservative LC (arising from the identical inter-planar spacing of the $(01\bar{1})_{hex}$ and $(01)_{sq}$ planes), can be fully accommodated. In other words, the system has achieved an average transformation strain $\langle\varepsilon_{transform}\rangle$ close to zero with the non-conservative LCs.

4.4. Limitation of the model

It should be pointed out that in the PFC model employed in the current study, the molar density of a phase and its lattice constant (i.e., site density) are independent. For example, for the same molar density of a given phase, the lattice constant will vary with the choice of k_1 in Eq. (2). This may lead to an unphysical situation where the single site occupation probability exceeds unity. In the currently study, however, the reference density ρ_L or the dimensional lattice parameter of the high temperature hexagon phase can always be chosen such that the single site occupation probability does not exceed unity and, then, when it transforms to the square phase at low temperatures the occupation probability can only decrease because of the increase in lattice site density, as have been shown in the simulations and discussed above.
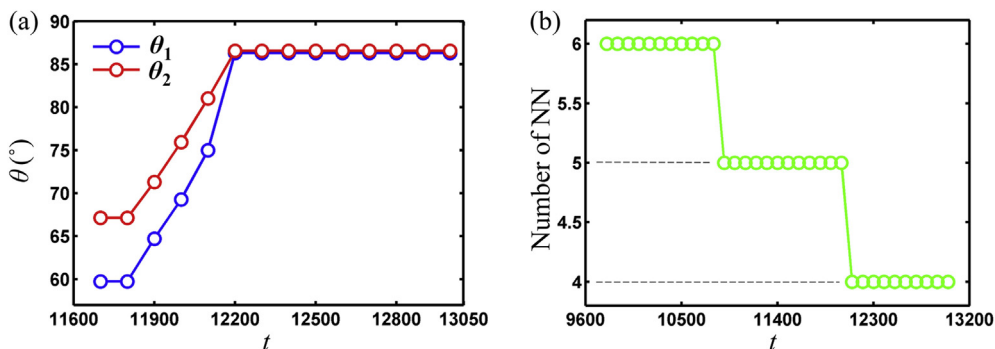
Fig. 9. (a) Variations of angles θ_1 and θ_2 (indicated in Fig. 4(a)) and (b) number of NN of the gold-colored atomic site (shown in Fig. 4) as function of time. (For interpretation of the references to colour in this figure legend, the reader is referred to the web version of this article.)
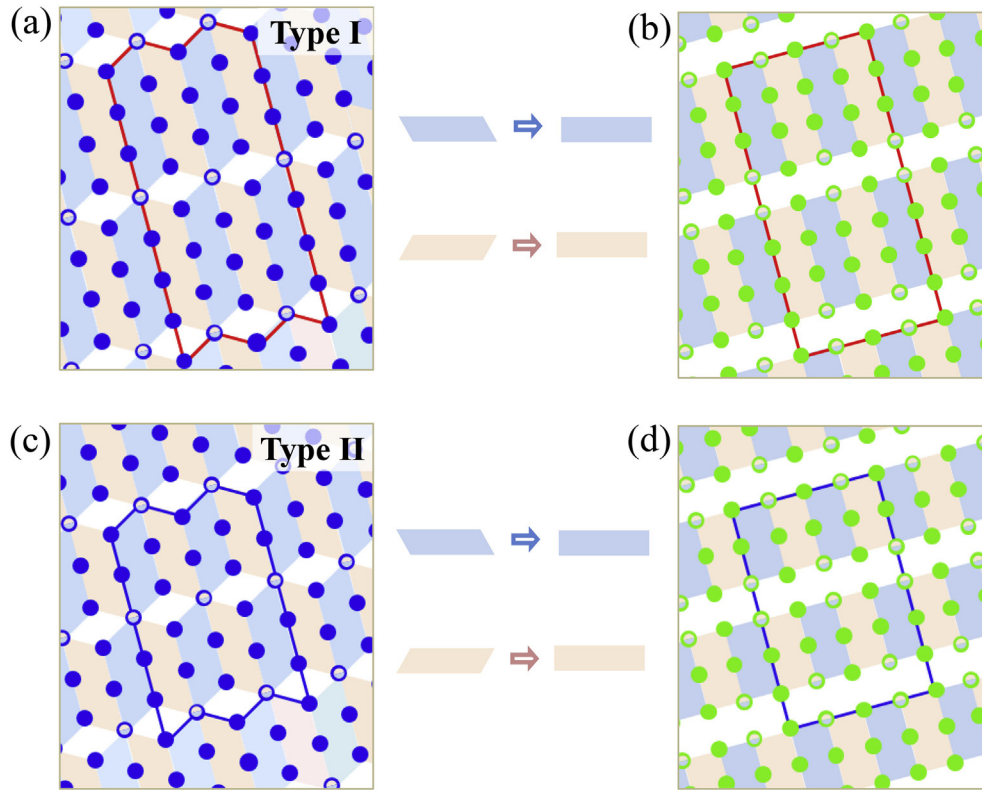
Fig. 10. Spatial arrangement of two opposite shearing zones (indicated by the light orange and blue background colors) involved during the hexagon to square structural transformation. (a) and (b) correspond to Type I arrangement with the shearing zones of length $3a_{hex}$, as indicated by the red boxes. (c) and (d) correspond to Type II arrangement with the shearing zones of length $2a_{hex}$, as indicated by the blue boxes. The one-to-two LC is among the open-circle sites on the two lattices. The two types of shear zones correspond to the two terrace sizes identified in Fig. 4(a). (For interpretation of the references to colour in this figure legend, the reader is referred to the web version of this article.)

5. Conclusion

In summary, a complete atomic picture of diffusional migration of a terrace-step phase boundary in a solid state phase transformation is provided for the first time, which has significant implications both theoretically and experimentally. First of all, the non-conservative LCs provides a generalized description for diffusional transformations, in particular where appreciable molar volume difference is involved. Furthermore, the non-conservative interface migration can be exploited as a new route for designing radiation-tolerant materials by accommodating the radiation-induced point defects. Secondly, in contrast to the conventional *synchronized* glide of SLs in order to preserve the inclination of the habit planes, a GL has been identified in our simulation. This may help to unveil the actual migration mechanism of planar interfaces during structural phase transformations such as the orthorhombic/tetragonal to monoclinic transformation in zirconia [10]. Thirdly, the opposite shearing mechanism found in this study provides a new way of eliminating transformation strain during diffusional structural transformations. The idea that the Frank-Bilby dislocation content [13] is divided into two groups that move differently is also used to explain stress-driven grain boundary migration that generates uniaxial plastic strain [47].

Lastly, by taking advantage of the efficiency of the FE-NEB technique in exploring the free energy landscape of PFC, a new approach capable of finding critical nucleus configurations with atomistic resolution and the corresponding activation energies are developed for both homogeneous and heterogeneous nucleation events.

Appendix A. Free energy densities for liquid, square and hexagon phases

By substituting the density field $n(\mathbf{r})$ for each phase as described before into Eq. (1), the corresponding free energy densities can be calculated as,

$$f_{liq} = \frac{1}{2}\overline{n}^2 - \frac{\eta}{6}\overline{n}^3 + \frac{\nu}{12}\overline{n}^4 - \frac{1}{2}\widehat{C}_2(0)\overline{n}^2 \tag{A1}$$

$$f_{sq} = a_1\left(A_{sq}^1\right)^4 + a_1\left(A_{sq}^2\right)^4 + b_1\left(A_{sq}^1\right)^2\left(A_{sq}^2\right)^2 + c_1\left(A_{sq}^1\right)^2\left(A_{sq}^2\right) + d_1\left(A_{sq}^1\right)^2 + e_1\left(A_{sq}^2\right)^2 + f_1 \tag{A2}$$

$$f_{hex} = a_2 A_{hex}^4 + b_2 A_{hex}^3 + c_2 A_{hex}^2 + d_2 \tag{A3}$$

where the coefficients are,

$$a_1 = 3\nu$$
$$b_1 = 12\nu$$
$$c_1 = 8\nu\bar{n} - 4\eta$$
$$d_1 = 2 - 2\eta\bar{n} + 2\nu\bar{n}^2 - 2\widehat{C}_2(k_1)$$
$$e_1 = 2 - 2\eta\bar{n} + 2\nu\bar{n}^2 - 2\widehat{C}_2(k_2)$$
$$f_1 = \frac{1}{2}\bar{n}^2 - \frac{\eta}{6}\bar{n}^3 + \frac{\nu}{12}\bar{n}^4 - \frac{1}{2}\widehat{C}_2(0)\bar{n}^2 \tag{A4}$$
$$a_2 = 15/2\nu$$
$$b_2 = 2\eta - 4\nu\bar{n}$$
$$c_2 = 3 - 3\eta\bar{n} + 3\nu\bar{n}^2 - 3\widehat{C}_2(k_1)$$
$$d_2 = \frac{1}{2}\bar{n}^2 - \frac{\eta}{6}\bar{n}^3 + \frac{\nu}{12}\bar{n}^4 - \frac{1}{2}\widehat{C}_2(0)\bar{n}^2$$

Appendix B. Crystallographic calculations of hexagon to square transformation

The base vectors of the hexagon matrix and the 3 deformation variants (DV), as indicated by blue and green arrows in Fig. 6, are expressed in an orthonormal coordinates as,

$$\boldsymbol{a}_1^{hex} = \begin{pmatrix} \frac{2}{\sqrt{3}} \\ 0 \end{pmatrix}, \ \boldsymbol{a}_2^{hex} = \begin{pmatrix} \frac{1}{\sqrt{3}} \\ 1 \end{pmatrix}, \ \boldsymbol{a}_1^{DV_1} = \begin{pmatrix} 1 \\ 0 \end{pmatrix}, \ \boldsymbol{a}_2^{DV_1}$$
$$= \begin{pmatrix} 0 \\ 1 \end{pmatrix}, \ \boldsymbol{a}_1^{DV_2} = \begin{pmatrix} 1 \\ 0 \end{pmatrix}, \ \boldsymbol{a}_2^{DV_2} = \begin{pmatrix} 1 \\ 1 \end{pmatrix}, \ \boldsymbol{a}_1^{DV_3} = \begin{pmatrix} \sqrt{2} \\ 0 \end{pmatrix}, \ \boldsymbol{a}_2^{DV_3}$$
$$= \begin{pmatrix} \frac{\sqrt{2}}{2} \\ \frac{\sqrt{2}}{2} \end{pmatrix}$$

and the corresponding reciprocal vectors in Fig. 5 are determined as,

$$\boldsymbol{g}_1^{hex} = \begin{pmatrix} \frac{\sqrt{3}}{2} \\ -\frac{1}{2} \end{pmatrix}, \ \boldsymbol{g}_2^{hex} = \begin{pmatrix} 0 \\ 1 \end{pmatrix}, \ \boldsymbol{g}_1^{DV_1} = \begin{pmatrix} 1 \\ 0 \end{pmatrix}, \ \boldsymbol{g}_2^{DV_1} = \begin{pmatrix} 0 \\ 1 \end{pmatrix}, \ \boldsymbol{g}_1^{DV_2}$$
$$= \begin{pmatrix} 0 \\ 1 \end{pmatrix}, \ \boldsymbol{g}_2^{DV_2} = \begin{pmatrix} 1 \\ -1 \end{pmatrix}, \ \boldsymbol{g}_1^{DV_3} = \begin{pmatrix} \frac{\sqrt{2}}{2} \\ -\frac{\sqrt{2}}{2} \end{pmatrix}, \ \boldsymbol{g}_2^{DV_3} = \begin{pmatrix} 0 \\ \sqrt{2} \end{pmatrix},$$

According to the O-line theory [11,48], the starting transformation matrix $\boldsymbol{A}_{o,i}^*$ linking the hexagon matrix and the DV is given by,

$$\boldsymbol{A}_{o,i}^* = \left[\boldsymbol{g}_1^{DV_i} \boldsymbol{g}_2^{DV_i}\right] \left[\boldsymbol{g}_1^{hex} \boldsymbol{g}_2^{hex}\right]^{-1} (i = 1-3) \tag{A5}$$

where the symbol '*' represents the matrix operation in reciprocal space and the index i denote the i-th deformation variant hereafter. During the calculations, the reference lattice is chosen as hexagon

lattice. Substituting the related reciprocal vectors into Eq. (A5), the above transformation matrices are calculated as,

$$\boldsymbol{A}_{o,1}^* = \begin{bmatrix} \frac{2}{\sqrt{3}} & 0 \\ \frac{1}{\sqrt{3}} & 1 \end{bmatrix}, \ \boldsymbol{A}_{o,2}^* = \begin{bmatrix} \frac{2}{\sqrt{3}} & 0 \\ -\frac{1}{\sqrt{3}} & 1 \end{bmatrix}, \ \boldsymbol{A}_{o,3}^* = \begin{bmatrix} \frac{\sqrt{6}}{3} & 0 \\ 0 & \sqrt{2} \end{bmatrix},$$

In order to form invariant lines [48], the final transformation matrix $\boldsymbol{A}_{o,i}^*$ needs to be acted by a rotation operation $\boldsymbol{R}_{i,j}^*$,

$$\boldsymbol{A}_{i,j}^* = \boldsymbol{R}_{i,j}^* \boldsymbol{A}_{o,i}^* (i = 1-3, \ j = 1, 2) \tag{A6}$$

where the matrix $\boldsymbol{A}_{i,j}^*$ describes the transformation from the hexagon lattice to the final orientation variant (OV). The index j denotes two different rotation matrix $\boldsymbol{R}_{i,j}^*$ associated with the transformation matrix $\boldsymbol{A}_{O,i}^*$. Required by the invariant line condition that one of eigenvalues of $\boldsymbol{A}_{i,j}^*$ should be one, i.e. $\left|\boldsymbol{I} - \boldsymbol{A}_{i,j}^*\right| = 0$, the rotation angles ϕ of rotation matrix $\boldsymbol{R}_{i,j}^*$ can be solved as (counter-clockwise rotation being positive),

$$\phi\left(\boldsymbol{R}_{1,1}^*\right) = -30°, \ \phi\left(\boldsymbol{R}_{1,2}^*\right) = 0°, \ \phi\left(\boldsymbol{R}_{2,1}^*\right) = 0°, \ \phi\left(\boldsymbol{R}_{2,2}^*\right)$$
$$= 30°, \ \phi\left(\boldsymbol{R}_{3,1}^*\right) = -15°, \ \phi\left(\boldsymbol{R}_{3,2}^*\right) = 15°$$

where the rotation starts from the orientation specified by their original DVs.

Since the habit plane is defined by the intersection of two pairs of correlated principal planes (containing at least two Burgers vectors [11]), the normal $\boldsymbol{n}$ of the habit plane equals to the displacement vector $\Delta\boldsymbol{g}$ between any one pair of them, which can be given by Refs. [11,48],

$$\Delta\boldsymbol{g}_{i,j} = (\boldsymbol{I} - \boldsymbol{A}_{i,j}^*)\boldsymbol{g}_P, \ (i = 1-3, j = 1, 2) \tag{A7}$$

where $\boldsymbol{g}_P$ refers to the principal reciprocal vector defined in hexagon lattice, i.e., $\boldsymbol{g}_1^{hex}$ or $\boldsymbol{g}_2^{hex}$. Thus the habit plane normal $\boldsymbol{n}$ is obtained as [49–51],

$$\boldsymbol{n}_{1,1} = \begin{pmatrix} -0.134 \\ -0.5 \end{pmatrix}, \ \boldsymbol{n}_{1,2} = \begin{pmatrix} -0.5 \\ 0.134 \end{pmatrix}, \ \boldsymbol{n}_{2,1} = \begin{pmatrix} 0.5 \\ 0.134 \end{pmatrix}, \ \boldsymbol{n}_{2,2}$$
$$= \begin{pmatrix} -0.1340 \\ 0.5 \end{pmatrix}, \ \boldsymbol{n}_{3,1} = \begin{pmatrix} 0.366 \\ -0.366 \end{pmatrix}, \ \boldsymbol{n}_{3,2} = \begin{pmatrix} -0.366 \\ -0.366 \end{pmatrix},$$

And the inclination angles φ between the habit plane and x-axis are converted to be $\varphi = 75°, -15°, 15°, -75°, -45°$ and $45°$.

Moreover, the unit height h_{GL} between two adjacent habit planes can be determined to be 1.932 following the relation $h_{GL} = 1/|\boldsymbol{n}|$ or $2h_{SL}$ in terms of the unit height of SL as shown in Fig. 8.

References

[1] H.I. Aaronson, J.P. Hirth, B.B. Rath, C.M. Wayman, General discussion sessions of the pacific rim conference on the roles of shear and diffusion in the formation of plate-shaped transformation products, Metall. Mater. Trans. 25A (1994) 2655–2673.
[2] D.A. Porter, K.E. Easterling, Phase Transformations in Metals and Alloys, Chapman and Hall, New York, 1992.
[3] A.P. Sutton, R.W. Balluffi, Interfaces in Crystalline Materials, Clarendon Press, Oxford, 1995.
[4] M.S. Wechsler, D.S. Liberman, T.A. Read, On the theory of the formation of martensite, Trans. AIME 197 (1953) 1503–1515.
[5] J.S. Bowles, J.K. Mackenzie, The crystallography of martensite transformations I, Acta Metall. 2 (1954) 129–137.
[6] F.C. Frank, Martensite, Acta Metall. 1 (1953) 15–21.
[7] W. Bollmann, Crystal defects and Crystalline Interfaces, Springer, Berlin, 1970.
[8] U. Dahmen, Surface relief and the mechanism of a phase transformation, Scr. Metall. 21 (1987) 1029–1034.
[9] M.G. Hall, H.I. Aaronson, Formation of invariant plane-strain and tent-shaped

surface reliefs by the diffusional ledge mechanism, Metall. Mater. Trans. 25A (1994) 1923—1931.

[10] Y.H. Chiao, I.W. Chen, Martensitic growth in ZrO_2 — an *in situ*, small particle, TEM s study of a single-interface transformation, Acta Metall. Mater. 38 (1990) 1163—1174.

[11] W.Z. Zhang, G.C. Weatherly, On the crystallography of precipitation, Prog. Mater. Sci. 50 (2005) 181—292.

[12] M.X. Zhang, P.M. Kelly, Crystallographic features of phase transformations in solids, Prog. Mater. Sci. 54 (2009) 1101—1170.

[13] J.P. Hirth, R.C. Pond, R.G. Hoagland, X.Y. Liu, J. Wang, Interface defects, reference spaces and the Frank-Bilby equation, Prog. Mater. Sci. 58 (2013) 749—823.

[14] J.F. Nie, Crystallography and Migration Mechanisms of Planar Interphase Boundaries, vol. 52, 2004, pp. 795—807.

[15] J.F. Nie, ge-to-edge matching of lattice planes and coupling of crystallography and migration mechanisms of planar interfaces, Metall. Mater. Trans. 37A (2006) 841—849.

[16] J.F. Nie, Orientation relationship, shape change and their traces in electron diffraction patterns and high-resolution transmission electron microscopy images, Acta Mater. 56 (2008) 3169—3176.

[17] J.W. Christian, Lattice correspondence, atomic site correspondence and shape change in "diffusional-displacive" phase transformations, Prog. Mater. Sci. 42 (1997) 101—108.

[18] J.M. Howe, Atomic site correspondence and surface relief in the formation of plate-shaped transformation products, Metall. Mater. Trans. 25A (1994) 1917—1922.

[19] P. Chalermkarnnon, H. Araki, Y. Shirai, Excess vacancies induced by disorder-order phase transformation in Ni_3Fe, Mater. Trans. 43 (2002) 1486—1488.

[20] A.D. Smigelskas, E.O. Kirkendall, Zinc diffusion in alpha brass, Trans. AIME 171 (1947) 130—142.

[21] K.R. Elder, M. Katakowski, M. Haataja, M. Grant, Modelling elasticity in crystal growth, Phys. Rev. Lett. 88 (2002) 245701.

[22] P. Stefanovic, M. Haataja, N. Provatas, Phase-field crystals with elastic interactions, Phys. Rev. Lett. 96 (2006) 225504.

[23] M. Greenwood, N. Provatas, J. Rottler, Free energy functionals for efficient phase field crystal modeling of structural phase transformations, Phys. Rev. Lett. 105 (2010) 045702.

[24] H. Emmerich, H. Löwen, R. Wittkowski, T. Gruhn, G.I. Tóth, G. Tegze, L. Gránásy, Phase-field-crystal models for condensed matter dynamics on atomic length and diffusive time scales: an overview, Adv. Phys. 61 (2012) 665—743.

[25] C. Shen, J. Li, Y. Wang, Finding critical nucleus in solid-state transformations, Metall. Mater. Trans. 39A (2007) 976—983.

[26] S. Sarkar, J. Li, W.T. Cox, E. Bitzek, T.J. Lenosky, Y. Wang, Finding activation pathway of coupled displacive-diffusional defect processes in atomistics: dislocation climb in fcc copper, Phys. Rev. B 86 (2012) 014115.

[27] Y. Wang, J. Li, Phase field modeling of defects and deformation, Acta Mater. 58 (2010) 1212—1235.

[28] K.A. Wu, A. Karma, Phase-field crystal modeling of equilibrium bcc-liquid interfaces, Phys. Rev. B 76 (2007) 184107.

[29] S. Tang, Z.J. Wang, Y.L. Guo, J.C. Wang, Y.M. Yu, Y.H. Zhou, Orientation selection process during the early stage of cubic dendrite growth, A Phase-field Cryst. study 60 (2012) 5501—5507.

[30] Y.J. Gao, L.L. Huang, Q.Q. Deng, W.Q. Zhou, Z.R. Luo, K. Lin, Phase Field Crystal Simulation of Dislocation Configuration Evolution in Dynamic Recovery in Two Dimensions, vol. 117, 2016, pp. 238—251.

[31] C. Kubstrup, H. Herrero, C. Pérez-García, Fronts between hexagons and squares in a generalized Swift-Hohenberg equation, Phys. Rev. E 54 (1996) 1560—1569.

[32] H. Sakaguchi, H.R. Brand, A modulation mediated hexagon-rectangle transition in pattern formation systems, Phys. Lett. A 227 (1997) 209—215.

[33] B. Abou, J.E. Wesfreid, S. Roux, The normal field instability in ferrofluids: hexagon-square transition mechanism and wavenumber selection, J. Fluid Mech. 416 (2000) 217—237.

[34] N. Matsushita, T. Ohta, Kinetics of square-hexagonal transformation in periodic domain structures, J. Phys. Soc. Jpn. 67 (1998) 1973—1981.

[35] Y. Enomoto, K. Oba, Y. Hayase, T. Ohta, Square-hexagonal transformation of periodic domain structures in a conserved system, J. Phys. Soc. Jpn. 70 (2001) 2939—2947.

[36] V. Fallah, J. Stolle, N. Ofori-Opoku, S. Esmaeili, N. Provatas, Phase-field crystal modeling of early stage clustering and precipitation in metal alloys, Phys. Rev. B 86 (2012) 134112.

[37] V. Fallah, N. Ofori-Opoku, J. Stolle, N. Provatas, E. Esmaeili, Simulation of early-stage clustering in ternary metal alloys using the phase-field crystal method, Acta Mater. 61 (2013) 3653—3666.

[38] G. Henkelman, B.P. Uberuaga, H. Jónsson, A climbing image nudged elastic band method for finding saddle points and minimum energy paths, J. Chem. Phys. 113 (2000) 9901—9904.

[39] G. Henkelman, H.J. Jónsson, Improved tangent estimate in the nudged elastic band method for finding minimum energy paths and saddle points, J. Chem. Phys. 113 (2000) 9978—9985.

[40] H. Humadi, J.J. Hoyt, N. Provatas, Phase-field-crystal study of solute trapping, Phys. Rev. E 87 (2013) 022404.

[41] D. Qiu, M.X. Zhang, P.M. Kelly, T. Furuhara, Discovery of plate-shaped athermal ω phase forming pairs with α′ martensite in a Ti-5.26 wt.%Cr alloy, Scr. Mater. 69 (2013) 752—755.

[42] N. Miyano, H. Fujiwara, K. Ameyama, G.C. Weatherly, Preferred orientation relationship of intra- and inter-granular precipitates in titanium alloys, Mater. Sci. Eng. A 333 (2002) 85—91.

[43] R.W. Balluffi, A. Brokman, A.H. King, CSL/DSC lattice model for general crystal-crystal boundaries and their line defects, Acta Metall. 30 (1982) 1453—1470.

[44] J.K. Chen, W.T. Reynolds Jr., The role of atomic matching and lattice correspondence in the selection of habit planes, Acta Mater. 45 (1997) 4423—4430.

[45] Y. Gao, R. Shi, J.F. Nie, S.A. Dregia, Y. Wang, Group theory description of transformation pathway degeneracy in structural phase transformations, Acta Mater. 109 (2016) 353—363.

[46] Variation of angle θ arising from spatial discretization process, termed as $\Delta\theta$, can be estimated using relation $\Delta\theta = \text{actan}(\Delta x/a_{sq}) = 5.7°$, where $\Delta x = 0.1$ and $a_{sq} = 1$.

[47] H.X. Zong, X.D. Ding, T. Lookman, J. Li, J. Sun, Uniaxial stress-driven coupled grain boundary motion in hexagonal close-packed metals: a molecular dynamics study, Acta Mater. 82 (2015) 295—303.

[48] J. Wu, W.Z. Zhang, X.F. Gu, A two-dimensional analytical approach for phase transformations involving an invariant line strain, Acta Mater. 57 (2009) 635.

[49] Y. Gao, L. Casalena, M.L. Bowers, R.D. Noebe, M.J. Mills, Y. Wang, An origin of functional fatigue of shape memory alloys, Acta Mater. 126 (2017) 389—400.

[50] Y. Gao, N. Zhou, D. Wang, Y. Wang, Pattern formation during cubic to orthorhombic martensitic transformations in shape memory alloys, Acta Mater. 68 (2014) 93—105.

[51] Y. Gao, H. Liu, R. Shi, N. Zhou, Z. Xu, Y. Zhu, J.-F. Nie, Y. Wang, Simulation study of precipitation in an Mg-Y-Nd alloy, Acta Mater. 60 (2012) 4819—4832.